PHYSICAL REVIEW A **109**, 013703 (2024)

Optical sideband generation in a nonlinear-magnon-mediated cavity

Yilou Liu,[1,2,*] Dongdong Yang,[1] Fengyun Chai,[3] Yu Xu,[1] Fulong Cui,[1] and Xiao-Tao Xie[1,†]
[1]*School of Physics and Information Technology, Shaanxi Normal University, Xi'an 710119, China*
[2]*Xi'an Key Laboratory of Optical Information Manipulation and Augmentation, Xi'an 710119, China*
[3]*Xi'an Institute of Space Radio Technology, Xi'an 710100, China*

(Received 19 September 2023; accepted 18 December 2023; published 8 January 2024;
corrected 21 March 2024)

We investigate optical sideband generation via the nonlinear magnon in a hybrid cavity-optomagnonical system consisting of a yttrium iron garnet sphere, a microwave copper cavity, and an optical cavity. By using a perturbation method to solve the nonlinear Heisenberg-Langevin equations, we obtain the analytical formulation of the nonlinear-magnon-induced optical second-order sideband (OSS) generation. It is found that the number of peaks in the OSS spectrum can change from 2 to 4 with the increase of the effective optical cavity-magnon coupling strength (EOCCS) within the experimental parameter range, which is caused by the gradual increase in overlap between the first- and second-order spectra. Moreover, the results show that the maximum value of the OSS will appear with an increase of the EOCCS, and the microwave cavity-magnon coupling strength (MCCS) will regulate the size and location of the maximum value. Subsequently, the output spectrum of the optical high-order sidebands is investigated using numerical simulations to demonstrate the modulation behavior of the OSS by the EOCCS and MCCS. In addition to providing insight into the interaction of the magnon with a microwave and light, our results may offer a new perspective for the development and design of microwave-controlled optical frequency combs.

DOI: 10.1103/PhysRevA.109.013703

I. INTRODUCTION

Cavity optomagnonics [1–3], which is the study of the interaction between magnetism and light, has recently become a focus of extensive research. The magnons, as the quanta of collective spin excitations in yttrium iron garnet (YIG) magnetic material, have high spin density, low damping rate, and long coherence time, which provide a completely new platform for cavity optomagnonics [4–6]. Experimentally, strong and ultrastrong couplings between magnons and microwave photons have been realized via magnetic dipole interaction [7,8]. Some interesting phenomena have been observed in the microwave photon-magnon coupling system, such as the magnon Kerr effect [9,10], non-Hermitian physics [11–14], optical chaos [15], and dissipative coupling [16,17]. In previous studies, the coupling effects between magnons and photons in the optical frequency range mainly focused on the Faraday effect [1]. In this case, the electromagnetically induced transparency effect, the Purcell effect, and the Brillouin scattering effect were observed [18–21]. Based on the interaction of the magnon mode with optical and microwave modes, conversion [22–25] and entanglement [26–29] between microwave and optical fields have become possible.

The generation of the optical sideband is an essentially nonlinear phenomenon that can be considered as a parametric process [30]. As is well known, the equidistant optical sideband spectra come from frequency combs [31]. Many methods for generating frequency combs have been proposed as research has progressed, for example, optomechanical frequency combs [32] and optomagnonic frequency combs [33]. In addition, frequency combs have also been theoretically predicted and experimentally demonstrated in the area of spin waves [34,35]. The study of optical sideband generation has thus become an essential component in the field of precision measurement [31]. The study of high-order sidebands has been reported in a hybrid optomechanical system [30,36,37], a hybrid optomagnonical system [38–40], an atom-microcavity coupling hybrid system [41], and semiconductors [42,43]. The study of optical sidebands in the hybrid cavity-optomagnonical system of light-magnetic material interaction opens up a new direction for precision measurement. Despite the similarities between cavity optomechanics [44] and cavity optomagnonics in many aspects, the direct analysis of optical sideband generation in the optical range through a perturbation method [30] and the influence of magnon Kerr nonlinearity [9,10,45] has not been well studied.

In this work we propose an intriguing scheme to realize the interaction of a magnon with an optical (and microwave) photon in a hybrid cavity-optomagnonical system consisting of a single small YIG crystal sphere, a three-dimensional (3D) rectangular copper cavity, and an optical cavity with two mirrors. By using a perturbation method, we solve the nonlinear Heisenberg-Langevin equations and obtain exact analytical forms of nonlinear-magnon-induced optical second-order sideband (OSS) generation. The simulation results show that the number of peaks in the OSS spectrum can change from 2 to 4 with an increase of the effective optical cavity-magnon coupling strength (EOCCS) within the experimental parameter range. The splitting phenomenon is mainly caused by the gradual increase in overlap between the

---

[*] yilouliu@163.com

[†] xtxie@snnu.edu.cn

2469-9926/2024/109(1)/013703(8)

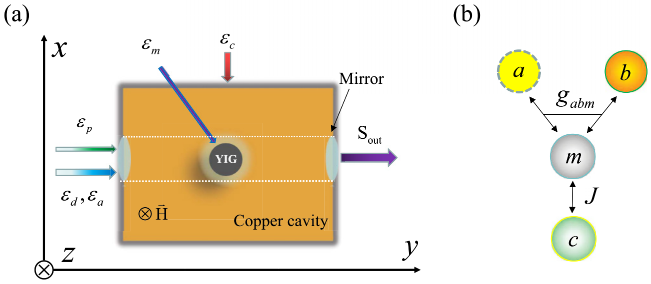

FIG. 1. (a) Schematic diagram of a hybrid cavity-optomagnonical system. (b) Equivalent mode-coupling model of the TM optical cavity mode a, the TE optical cavity mode b, the magnon mode m, and the microwave cavity mode c. The optical cavity mode interacts with the magnon mode through linear and quadratic magneto-optical coupling [18], i.e., g_{abm}. The microwave cavity mode and magnon mode frequency ranges are close enough to allow direct coupling, i.e., J.

first- and second-order spectra. As the EOCCS increases, a maximum value of OSS will be reached, while the microwave cavity-magnon coupling strength (MCCS) can regulate the size and location of the maximum value. Furthermore, we give the output spectrum of the optical high-order sidebands by numerical simulations. Our scheme may offer new prospects for the development of optomagnonic frequency combs and other precision measurements.

II. MODEL AND EQUATIONS

The physical model used in our study is shown in Fig. 1, which consists of a YIG sphere, a microwave 3D copper cavity, and an optical cavity. The YIG sphere is located at the central intersection of a microwave cavity and an optical cavity. A uniform external magnetic field H is applied in the z direction to bias the YIG sphere. The microwave cavity and the YIG sphere are driven by the power of the microwave driving fields P_c and P_m, respectively. It should be pointed out that the YIG sphere can be driven directly by a loop drive antenna connected to the end of a superconducting microwave line for the current experimental operation [9]. The driving strength $\varepsilon_i = \sqrt{P_i/\hbar\omega_l}$ $(i = m, c)$, with ω_l the frequency of the driving field. The optical cavity is driven by two light control fields at frequency $\omega_{a,d}$ and probed by a weak light signal field at frequency ω_p, and their amplitudes are defined as $\varepsilon_j = \sqrt{P_j/\hbar\omega_j}$ $(j = a, d, p)$, with P_j the input power. The total Hamiltonian of the present hybrid system $(\hbar = 1)$ can be written as

$$\begin{aligned}\hat{H} =\ & \omega_a\hat{a}^\dagger\hat{a} + \omega_b\hat{b}^\dagger\hat{b} + \omega_m\hat{m}^\dagger\hat{m} + \omega_c\hat{c}^\dagger\hat{c} + K\hat{m}^\dagger\hat{m}\hat{m}^\dagger\hat{m}\\ & + g_{abm}(\hat{a}\hat{b}^\dagger\hat{m} + \hat{a}^\dagger\hat{b}\hat{m}^\dagger) + J(\hat{c} + \hat{c}^\dagger)(\hat{m} + \hat{m}^\dagger)\\ & + \sqrt{\kappa_c}(\hat{c}^\dagger\varepsilon_c e^{-i\omega_l t} + \text{H.c.})\\ & + \sqrt{\kappa_m}(\hat{m}^\dagger\varepsilon_m e^{-i\omega_l t} + \text{H.c.})\\ & + \sqrt{\kappa_a}(\hat{a}^\dagger\varepsilon_a e^{-i\omega_a t} + \text{H.c.})\\ & + \sqrt{\kappa_b}\big[\hat{b}^\dagger\big(\varepsilon_d e^{-i\omega_d t} + \varepsilon_p e^{-i\omega_p t}\big) + \text{H.c.}\big],\end{aligned} \tag{1}$$

where $\hat{a}$ $(\hat{a}^\dagger)$, $\hat{b}$ $(\hat{b}^\dagger)$, $\hat{m}$ $(\hat{m}^\dagger)$, and $\hat{c}$ $(\hat{c}^\dagger)$ are the annihilation (creation) operators of the TM optical cavity mode, TE optical cavity mode, magnon mode, and microwave cavity mode with frequencies ω_a, ω_b, ω_m, and ω_c, respectively. The term $K\hat{m}^\dagger\hat{m}\hat{m}^\dagger\hat{m}$ represents the magnon Kerr nonlinearity with the nonlinear coefficient. It is worth noting that the coefficient K is inversely proportional to the volume of the YIG sphere [45]. Here $g_{abm} = \nu\frac{c}{n_r}\sqrt{\frac{2}{n_{\text{spin}}V_{\text{sp}}}}$ is the coupling strength of the two optical modes and the magnon mode, where the Verdet constant $\nu = 3.77$ rad/cm, the refractive index $n_r = 2.19$, the spin density $n_{\text{spin}} = 2.1 \times 10^{28}$ m^{-3}, the speed of light in vacuum $c = 2.9979$ m/s, and V_{sp} is the volume of YIG. In addition, J is the coupling strength of the microwave cavity mode and the magnon mode and κ_a, κ_b, κ_m, and κ_c are the decay rates of the TM optical mode, TE optical mode, magnon mode, and microwave cavity mode, respectively.

For the sake of simplicity, we can linearize the interaction Hamiltonian $\hat{H}_{abm} = g_{abm}(\hat{a}\hat{b}^\dagger\hat{m} + \hat{a}^\dagger\hat{b}\hat{m}^\dagger)$ of the two (TM and TE) optical modes and the magnon mode. Under the condition in which the TM optical mode $\hat{a}$ is pumped by the light control field of frequency ω_a, the TM optical mode can be treated as a classical light field. So we can achieve $\hat{H}_{abm} = G(\hat{b}^\dagger\hat{m}e^{-i\omega_a t} + \hat{b}\hat{m}^\dagger e^{i\omega_a t})$, where $G = g_{abm}\alpha$, with α the average amplitude of the TM optical field. The Hamiltonian (1) becomes

$$\begin{aligned}\hat{H} =\ & \omega_b\hat{b}^\dagger\hat{b} + \omega_m\hat{m}^\dagger\hat{m} + \omega_c\hat{c}^\dagger\hat{c} + K\hat{m}^\dagger\hat{m}\hat{m}^\dagger\hat{m}\\ & + G\big(\hat{b}^\dagger\hat{m}e^{-i\omega_a t} + \hat{b}\hat{m}^\dagger e^{i\omega_a t}\big) + J(\hat{c} + \hat{c}^\dagger)(\hat{m} + \hat{m}^\dagger)\\ & + \sqrt{\kappa_c}\big(\hat{c}^\dagger\varepsilon_c e^{-i\omega_l t} + \text{H.c.}\big)\\ & + \sqrt{\kappa_m}\big(\hat{m}^\dagger\varepsilon_m e^{-i\omega_l t} + \text{H.c.}\big)\\ & + \sqrt{\kappa_b}\big[\hat{b}^\dagger\big(\varepsilon_d e^{-i\omega_d t} + \varepsilon_p e^{-i\omega_p t}\big) + \text{H.c.}\big].\end{aligned} \tag{2}$$

By applying the unitary transformation $\hat{U}(t) = \exp[-i(\omega_a + \omega_l)\hat{b}^\dagger\hat{b}t - i\omega_l\hat{m}^\dagger\hat{m}t - i\omega_l\hat{c}^\dagger\hat{c}t]$ and the rotating-wave approximation, the simplified Hamiltonian in Eq. (2) can be written in the form

$$\begin{aligned}\hat{H}' =\ & \Delta_b\hat{b}^\dagger\hat{b} + \Delta_m\hat{m}^\dagger\hat{m} + \Delta_c\hat{c}^\dagger\hat{c} + K\hat{m}^\dagger\hat{m}\hat{m}^\dagger\hat{m}\\ & + G(\hat{b}^\dagger\hat{m} + \hat{b}\hat{m}^\dagger) + J(\hat{c}\hat{m}^\dagger + \hat{c}^\dagger\hat{m})\\ & + \sqrt{\kappa_c}\varepsilon_c(\hat{c}^\dagger + \hat{c}) + \sqrt{\kappa_m}\varepsilon_m(\hat{m}^\dagger + \hat{m})\\ & + \sqrt{\kappa_b}\big[\hat{b}^\dagger\big(\varepsilon_d e^{-i\Delta_d t} + \varepsilon_p e^{-i\Delta_p t}\big) + \text{H.c.}\big],\end{aligned} \tag{3}$$

where $\Delta_b = \omega_b - \omega_a - \omega_l$, $\Delta_m = \omega_m - \omega_l$, $\Delta_c = \omega_c - \omega_l$, $\Delta_d = \omega_d - \omega_a - \omega_l$, and $\Delta_p = \omega_p - \omega_a - \omega_l$ are the detunings. This interaction in the optomagnetic system is subject to the rule of angular momentum and the energy conservation requirement, i.e., $\omega_b - \omega_a = \omega_m$ [21,46,47]. As noted above, we have assumed $\omega_m = \omega_c = \omega_b - \omega_a$; thus, we can obtain $\Delta_m = \Delta_c = \Delta_b$. To make the driving terms time independent, we consider the detuning $\Delta_d = 0$, i.e., $\omega_d = \omega_a + \omega_l = \omega_b - \Delta_b$.

According to the Heisenberg-Langevin equations (HLE) approach, the dynamic evolutions of the hybrid system can be described by

$$\begin{aligned}\dot{m} =\ & (-i\Delta_m - \kappa_m)m - iGb - iJc\\ & - i(2Km^*m + K)m - i\sqrt{\kappa_m}\varepsilon_m,\end{aligned} \tag{4}$$

$$\dot{b} = -(i\Delta_b + \kappa_b)b - iGm - i\sqrt{\kappa_b}\big(\varepsilon_d + \varepsilon_p e^{-i\Delta_p t}\big), \tag{5}$$

$$\dot{c} = (-i\Delta_c - \kappa_c)c - iJm - i\sqrt{\kappa_c}\varepsilon_c. \tag{6}$$

In this work we are interested in the mean response of the hybrid system to the probe field, so the operators can be reduced to their expectation values, viz., $\langle\hat{b}(t)\rangle \equiv b(t)$, $\langle\hat{m}(t)\rangle \equiv m(t)$, $\langle\hat{c}(t)\rangle \equiv c(t)$, $\langle\hat{b}^\dagger(t)\rangle \equiv b^*(t)$, $\langle\hat{m}^\dagger(t)\rangle \equiv m^*(t)$, and $\langle\hat{c}^\dagger(t)\rangle \equiv c^*(t)$. In this case, the quantum and thermal noise terms can be dropped due to $\langle\hat{b}_{\rm in}(t)\rangle = 0$, $\langle\hat{m}_{\rm in}(t)\rangle = 0$, and $\langle\hat{c}_{\rm in}(t)\rangle = 0$. It should be noted that the control field is proposed to be much stronger than the probe field in this article. In this case, the nonlinear equations (4)–(6) cannot be solved exactly, because the steady-state response contains an infinite number of components of different frequencies. Instead, the system is treated as a perturbed system and the perturbation method can be used to deal with Eqs. (4)–(6). The control field provides a steady-state solution of the system, while the probe field is treated as the small perturbation of the steady state [30,48]. To this end, the operators can be described by $b = b_s + \delta b$, $m = m_s + \delta m$, and $c = c_s + \delta c$, where b_s, m_s, and c_s are the steady-state solutions, respectively, and δb, δm, and δc express the corresponding small perturbation on steady-state solutions. The steady-state solutions of the HLEs are obtained as

$$m_s = \frac{iGb_s + iJc_s + i\sqrt{\kappa_m}\varepsilon_m}{-i\Delta_m - \kappa_m - i(2K|m_s|^2 + K)}, \tag{7}$$

$$b_s = \frac{iGm_s + i\sqrt{\kappa_b}\varepsilon_d}{-i\Delta_b - \kappa_b}, \tag{8}$$

$$c_s = \frac{iJm_s + i\sqrt{\kappa_c}\varepsilon_c}{-i\Delta_c - \kappa_c}. \tag{9}$$

We now consider the perturbation made by the probe field. By substituting these perturbation terms δb, δm, and δc into Eqs. (4)–(6), the perturbation HLEs can be obtained:

$$\begin{aligned}\delta\dot{m} = {} & (-i\Delta_m - \kappa_m)\delta m - iJ\delta c - iG\delta b - iK\delta m \\ & - 2iK(m_s)^2\delta m^* - 2iK{m_s}^*\delta m^2 \\ & - 4iK|m_s|^2\delta m - 4iKm_s\delta m^*\delta m,\end{aligned} \tag{10}$$

$$\delta\dot{b} = (-i\Delta_b - \kappa_b)\delta b - iG\delta m - i\sqrt{\kappa_b}\varepsilon_p e^{-i\Delta_p t}, \tag{11}$$

$$\delta\dot{c} = (-i\Delta_c - \kappa_c)\delta c - iJ\delta m. \tag{12}$$

To solve the term of the input probe field $\varepsilon_p e^{-i\Delta_p t}$, we assume that the perturbation terms δb, δm, and δc have the forms $\delta o = O_1^- e^{-i\Delta_p t} + O_1^+ e^{i\Delta_p t} + O_2^- e^{-2i\Delta_p t} + O_2^+ e^{2i\Delta_p t}$ ($o = b, m, c$ correspond to $O = B, M, C$, respectively). Here O_1^- (O_2^-) is the coefficient of the first- (second)-order upper sideband with the frequency $\omega_d + \Delta_p$ ($\omega_d + 2\Delta_p$) and O_1^+ (O_2^+) is the coefficient of the first- (second)-order lower sideband with the frequency $\omega_d - \Delta_p$ ($\omega_d - 2\Delta_p$). The first upper sideband is referred to as the anti-Stokes field and the first lower sideband is known as the Stokes field. In the present work we consider only the first- and second-order sidebands, while the high-order sidebands are ignored since they can be obtained in a similar procedure. For simplicity, we give only O_1^- (O_2^-) [O_1^+ (O_2^+); see the Appendix]. Substituting the above assume into Eqs. (10)–(12), we can get

$$M_1^- = \frac{G\sqrt{\kappa_b}\varepsilon_p f(i\Delta_p)^*}{\delta(i\Delta_p)[f(-i\Delta_p)f(i\Delta_p)^* - 4K^2|m_s|^4]}, \tag{13}$$

$$B_1^- = \frac{iGM_1^- + i\sqrt{\kappa_b}\varepsilon_p}{\delta(i\Delta_p)}, \tag{14}$$

$$C_1^- = \frac{iJM_1^-}{-i\Delta_c - \kappa_c + i\Delta_p}, \tag{15}$$

where $\delta(x) = -i\Delta_b - \kappa_b + x$ and $f(x) = i\Delta_m + \kappa_m + x + 4iK|m_s|^2 + iK + \frac{J^2}{i\Delta_c + \kappa_c + x} + \frac{G^2}{i\Delta_b + \kappa_b + x}$. We also can solve the equations and obtain B_2^- as

$$M_2^- = \frac{(m+n)(M_1^-)^2}{[f(-2i\Delta_p)f(2i\Delta_p)^* - 4K^2|m_s|^4][f(i\Delta_p)^*]^2}, \tag{16}$$

$$B_2^- = \frac{iGM_2^-}{\delta(2i\Delta_p)}, \tag{17}$$

$$C_2^- = \frac{iJM_2^-}{-i\Delta_c - \kappa_c + 2i\Delta_p}, \tag{18}$$

where

$$\begin{aligned}m = {} & 16iK^3(m_s)^*|m_s|^4 f(i\Delta_p)^* \\ & - 2iK(m_s)^*[f(i\Delta_p)^*]^2 f(2i\Delta_p)^*,\end{aligned} \tag{19}$$

$$\begin{aligned}n = {} & -16K^4(m_s)^*|m_s|^6 \\ & + 8K^2(m_s)^*|m_s|^2 f(i\Delta_p)^* f(2i\Delta_p)^*.\end{aligned} \tag{20}$$

Subsequently, according to the input-output notation $S_{\rm out} = S_{\rm in} - i\sqrt{\kappa_b}b$, the output transmission field can be expressed as

$$\begin{aligned}S_{\rm out} = {} & \vartheta_0 e^{-i\omega_d t} - \vartheta_1 e^{-i\omega_p t} - i\sqrt{\kappa_b}B_1^+ e^{-i(\omega_d - \Delta_p)t} \\ & - i\sqrt{\kappa_b}B_2^- e^{-i(\omega_d + 2\Delta_p)t} \\ & - i\sqrt{\kappa_b}B_2^+ e^{-i(\omega_d - 2\Delta_p)t},\end{aligned} \tag{21}$$

where $\vartheta_0 = \varepsilon_d - i\sqrt{\kappa_b}b_s$ and $\vartheta_1 = i\sqrt{\kappa_b}B_1^- - \varepsilon_p$. The transmission of the probe pulse can be defined as $t_p = \vartheta_1/\varepsilon_p$, with $|t_p|^2$ the optical transmission strength. The dimensionless quantities $\eta_2 = |i\sqrt{\kappa_b}B_2^-/\varepsilon_p|$ and $\beta_2 = |i\sqrt{\kappa_b}B_2^+/\varepsilon_p|$ can be defined to describe the conversion efficiency of the upper and lower OSSs, respectively. The output intensity of the optical sideband generation can be scaled about the strength of the input probe field. In the following, we will discuss η_2 in detail in response to the efficiency of the OSS, while the results for β_2 are not presented here as the properties are similar.

III. RESULTS AND DISCUSSION

In this section the generation and control of the optical sidebands are illustrated in the cavity-magnon hybrid system. Considering that the OSS is typical of high-order sidebands, the efficiency η_2 of the OSS will be discussed in detail. We first show the features of the OSS generation when the microwave cavity mode decouples with the magnon mode, i.e., $J = 0$. Figure 2 illustrates the conversion efficiency η_2 as a function of the EOCCS G and the detuning Δ_p. It should be pointed out that, with the increase of G, the conversion efficiency η_2 (%) reaches its maximum value near $G/\kappa = 0.32$, as shown by the white dashed line in Fig. 2. For ease of explanation and illustration, the EOCCS $G/\kappa = 0.32$ is

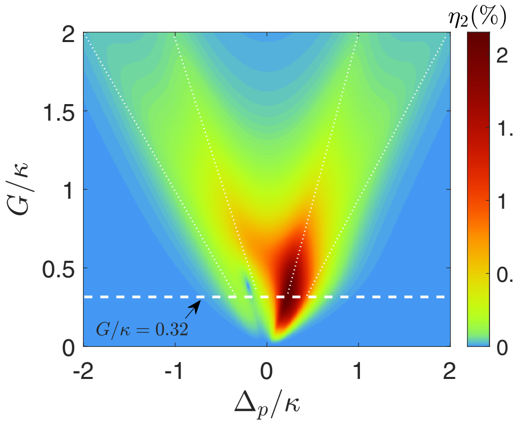

FIG. 2. Conversion efficiency η_2 (%) versus the detuning Δ_p/κ and the coupling strength G/κ for $\omega_m = 6.75$ GHz, $2\kappa_m = 1$ MHz, $2\kappa_b = 15$ MHz, $2\kappa_c/2\pi = 3.3$ MHz, $J = 0$, $K/2\pi = 10^{-6}$, $\Delta_c = \Delta_m = \Delta_b = 0$, $P_d = P_c = 15$ mW, $P_m = 0.05$ μW, $\lambda_d = 1550$ nm, $\varepsilon_p = 0.05\varepsilon_d$, and $\kappa = 10$ MHz.

taken as the boundary, defined as the weak-coupling–strong-coupling regime between the magnon mode and the TE optical cavity mode, respectively. In the weak-coupling regime G of Fig. 2, i.e., $G/\kappa < 0.32$, we can observe two asymmetrically highlighted regions appearing on the left and right sides of the detuned $\Delta_p = 0$ as the EOCCS increases. When the EOCCS G is pushed into the strong-coupling regime, i.e., $G/\kappa > 0.32$, it can be seen in Fig. 2 that four bright lines split from the red-yellow region, representing the four peak values of η_2. In addition, as the EOCCS G increases, the position of the sideband peaks moves away from $\Delta_p = 0$ and the peaks' values gradually decrease, as shown in Fig. 2.

For direct insight into the influence of the G on the OSS spectra and the transmission spectra, we show in Fig. 3 that the transmission $|t_p|^2$ of the probe field and the efficiency η_2 (%) of the OSS process vary with the detuning for different values of $G/\kappa = 0.3, 1, 2$. For the EOCCS $G = 0.3/\kappa$, the spectrum of $|t_p|^2$ shows two slightly asymmetry absorbed valleys and a transparent window near $\Delta_p/\kappa = 0$ [Fig. 3(a)]. Further, the OSS spectrum η_2 shown in Fig. 3(b) exhibits a line shape of two asymmetric peaks. The asymmetry of the OSS spectra arises from the constructive and destructive interference between the process of the direct OSS generation and the process of the up-converted first-order sideband [49]. From the two slightly asymmetric absorption valleys in Figs. 3(c) and 3(e) it can be observed that the transmission spectrum $|t_p|^2$ moves to both sides and the transparent window becomes wider with the increase of G. As G increases from 0.3κ to 1κ in Fig. 3(d), the spectrum of η_2 (%) displays two asymmetric peaks that shift towards both sides and the efficiency of η (%) is reduced rapidly. This indicates that the EOCCS $G/\kappa > 0.32$ suppresses the generation of the OSS. As G increases from 1κ to 2κ in Fig. 3(f), the spectrum of η_2 (%) displays asymmetric peaks that shift towards both sides, accompanied by the splitting of two peaks into four peaks, and the efficiency of η (%) is reduced rapidly.

Under the condition of the microwave cavity mode decoupling from the magnon mode (i.e., $\Delta_b = 0$ and $\Delta_m = 0$), the physical picture of the transmission $|t_p|^2$ spectrum splitting is rather clear, as shown in Figs. 3(a), 3(c), and 3(e). To explain this interesting phenomenon, we can express the eigenfrequencies by the magnon-photon coupling as [40]

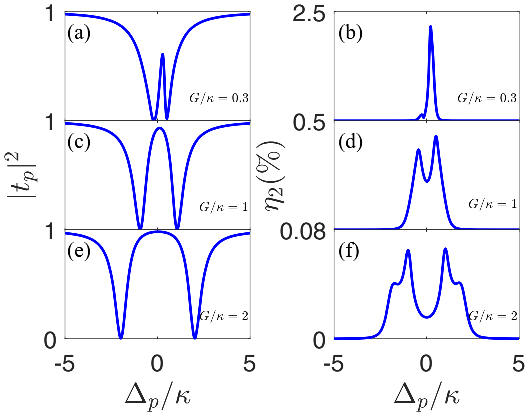

FIG. 3. Transmission rate of the probe pulse $|t_p|^2$ and the conversion efficiency η_2 (%) versus the detuning Δ_p/κ for (a) and (b) $G/\kappa = 0.3$, (c) and (d) $G/\kappa = 1$, and (e) and (f) $G/\kappa = 2$. The other parameters are the same as in Fig. 2.

$$\omega_\pm = \tfrac{1}{2}K\langle m^* m\rangle \pm \tfrac{1}{2}\sqrt{(K\langle m^* m\rangle)^2 + 4G^2}. \tag{22}$$

The OSS generation, as a parametric transformation based on the first-order sideband, is accompanied by more complex physical mechanisms. Therefore, we cannot explain the splitting of two peaks into four peaks mechanism of the OSS spectrum in Figs. 3(d) and 3(f). According to Eqs. (16)–(20), the OSS generation efficiency can be expressed as

$$\eta_2 = \left|\frac{-G\sqrt{\kappa_b}(m+n)F_1F_2}{\varepsilon_p}\right|, \tag{23}$$

where

$$F_1 = \frac{(M_1^-)^2}{[f(i\Delta_p)^*]^2}, \tag{24}$$

$$F_2 = \frac{1}{[f(-2i\Delta_p)f(2i\Delta_p)^* - 4K^2|m_s|^4]\delta 2}. \tag{25}$$

The expression (23) of the OSS clearly contains a first-order correlation term (24) and a second-order correlation term (25). It is worth noting that we consider that in the strong-coupling regime $G \gg K$, so the $m + n$ term can be approximated as a constant term. Then we can redefined the dimensionless quantities

$$\eta_2^1 = \sqrt{\left|\frac{-G\sqrt{\kappa_b}(m+n)}{\varepsilon_p}\right|}|F_1| \tag{26}$$

and

$$\eta_2^2 = \sqrt{\left|\frac{-G\sqrt{\kappa_b}(m+n)}{\varepsilon_p}\right|}|F_2| \tag{27}$$

of the conversion efficiency η_2 (%) just associated with the first-order term and the second-order term, respectively. The transmission rate of the probe pulse $|t_p|^2$ and the efficiency of η_2 (%), η_2^1, and η_2^2 are plotted versus the detuning Δ_p/κ

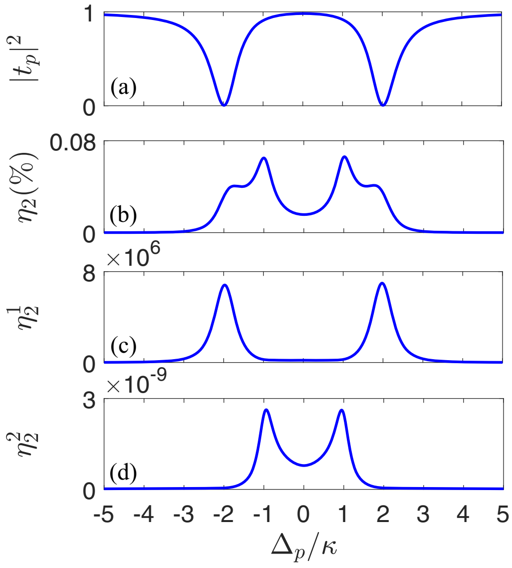

FIG. 4. Transmission rate of the probe pulse $|t_p|^2$ and the efficiency of η_2 (%), η_2^1, and η_2^2 versus the detuning Δ_p/κ for $G/\kappa = 2$ and the other parameters the same as in Fig. 2.

in Fig. 4. It can be seen in Fig. 4(c) that the spectrum of η_2^1 features a two-peak line shape at the position $\Delta_p/\kappa = \pm 2$. The positions of these two peaks correspond to the positions of the two absorption valleys of $|t_p|^2$ in Fig. 4(a) and the outer two peaks of η_2 (%) in Fig. 4(b). The spectrum of η_2^2 shown in Fig. 4(d) exhibits a two-peak line shape at the position $\Delta_p/\kappa = \pm 1$ corresponding to the positions of the inner two peaks of η_2 (%) in Fig. 4(b). This means that the splitting of the two peaks into four peaks shown by the spectrum of η_2 (%) is mainly due to the frequency difference between the first-order term and the second-order term during the parametric conversion process.

In the following, we investigate the effect of the MCCS J of the microwave cavity mode and the magnon mode on the generation of optical sidebands, i.e., $J \neq 0$. The conversion efficiency η_2 versus the detuning Δ_p and the MCCS J is plotted in Fig. 5. When $G/\kappa = 0.3$, it can be observed in Fig. 5(a) that as the MCCS J increases, the two asymmetric highlighted lines near $\Delta_p = 0$ split into four asymmetric highlighted lines, representing the four peaks of η_2. The physical mechanism of the two peaks splitting into four peaks can be seen from the expressions (24)–(27). We note that the lines with $\Delta_p > 0$ are brighter than the lines with $\Delta_p < 0$. Furthermore, as J increases, the position of the sideband peaks moves further from $\Delta_p = 0$ and the peak values steadily diminish. When the value of G is pushed into the strong-coupling regime, i.e., $G/\kappa = 2$, it can be seen from Fig. 5(b) that the four highlighted lines representing the four peaks of η_2 (%) gradually become brighter as J. This indicates that the OSS conversion efficiency increases gradually with the increase of J for the value of $G/\kappa = 2$.

In order to clearly show the effect of the MCCS J on the conversion efficiency η_2 whether the EOCCS G is in the weak-coupling or the strong-coupling regime, the maximal values of η_2 versus G with and without J are depicted in Fig. 6. In the absence of the MCCS J, the maximum value of η_2 at $G/\kappa = 0.32$ shows a single peak ($\eta_2^{\max} < 2.5\%$) that first increases exponentially and then decreases in inverse proportion. In contrast to the single-peak profile in a TE optical cavity-magnon coupling system, it can be seen from Fig. 6 that the peak profile of the maximum value of η_2 is frequency shifted toward the G strong coupling and is accompanied by a decrease in the peak when the MCCS J is included. It is worth noting that when $G/\kappa < 0.32$ the maximum value of η_2 increases with increasing G, and the growth rate of the maximum value of η_2 for $J/\kappa = 0$ is greater than the growth rate of the maximum value of η_2 for the MCCS $J/\kappa = 0.006$. When G is pushed into the regime $0.32 < G/\kappa < 0.8$, the

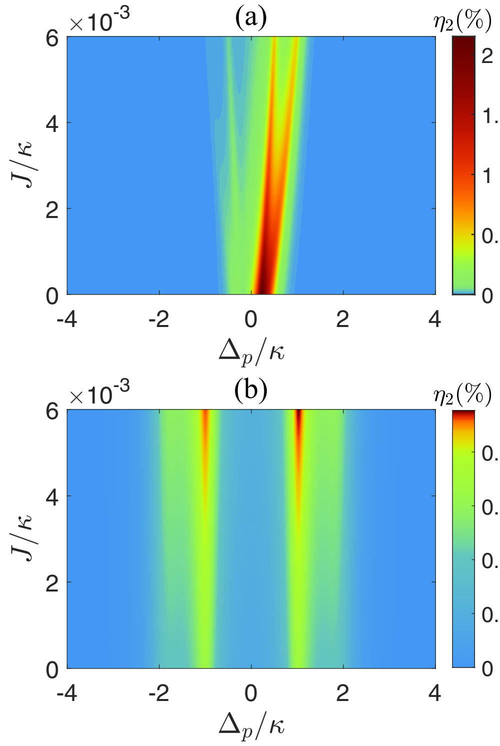

FIG. 5. Conversion efficiency η_2 (%) versus the detuning Δ_p/κ and the coupling strength J/κ for (a) $G = 0.3\kappa$ and (b) $G = 2\kappa$ and the other parameters the same as in Fig. 2.

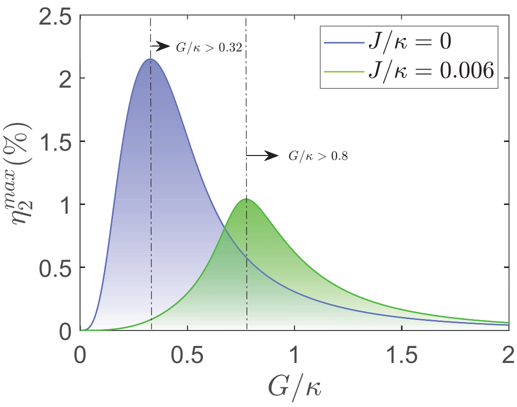

FIG. 6. Maximum efficiency of η_2 (%) as a function of the TE optical cavity-magnon coupling strength G/κ for two different situations, i.e., without J (violet line) and with J (green line). The other parameters are the same as in Fig. 2.

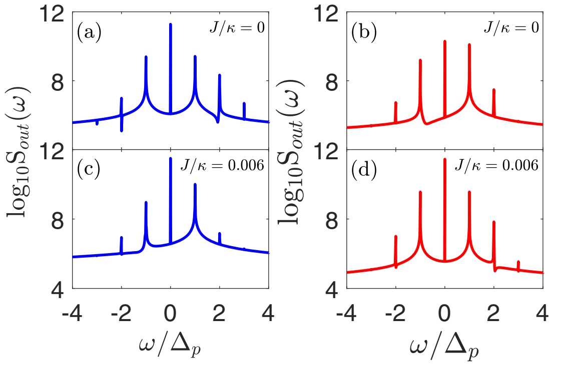

FIG. 7. Frequency spectrum output of the optical high-order sidebands (in logarithmic scale) under two different coupling strengths G and J for (a) and (c) $G/\kappa = 0.32$ and (b) and (d) $G/\kappa = 0.8$ and (a) and (b) $J/\kappa = 0$ and (c) and (d) $J/\kappa = 0.006$. The other parameters are the same as in Fig. 2.

maximum value of η_2 for $J/\kappa = 0$ decreases with increasing G; however, the maximum value of η_2 for $J/\kappa = 0.006$ continues to increase with increasing G. When G is pushed to $G/\kappa > 0.8$, the maximum value of η_2 decreases with increasing G. Interestingly, the maximum value of η_2 at the MCCS $J/\kappa = 0$ is consistently smaller than the maximum value of η_2 at $J/\kappa = 0.006$ as the EOCCS G increases. This makes it possible for us to control the optical sidebands by tuning the microwave field.

In all of the above discussion, we mainly focused on the OSS based on the analytical solution by a perturbation method. Next we turn to discuss the role of J and G in the optical high-order sideband generation. Figure 7 shows the output spectrum of the optical high-order sidebands by direct numerical simulation according to Eqs. (4)–(6). The frequency domain output spectrum can be obtained by the fast Fourier transform of S_{out}, i.e., $S(\omega) \propto |\int_{-\infty}^{\infty} S_{\text{out}}(t)e^{-i\omega t}dt|$, where ω is the spectroscopy frequency from the optical cavity field [37,38]. The observed optical higher-order sidebands are spaced at multiples of the beating frequency Δ_p between the driving components around the rotating frequency ω_d. This is analogous to generating a series of higher harmonics in the spectral density of a wandering respirator [50]. As a result, the frequency of the optical high-order sidebands of order n can be formulated by the relationship $\omega_n = \omega_d \pm n\Delta_p$, where n is the number of sidebands. It is obvious that the zeroth-order signal ($n = 0$) corresponds to the control field. The first-order upper sideband at the probe pulse frequency $\omega_d + \Delta_p$ originates from anti-Stokes processes, while the second-order upper sideband with frequency $\omega_d + 2\Delta_p$ stems from the magnon nonlinearity in the present system. The optical higher-order sidebands are caused by the coupling and beating between the nonlinear magnon and optical (microwave) cavity modes in resonance, as shown in Fig. 7. The amplitude of the optical high-order sidebands decreases rapidly as the order number of the sideband increases gradually. Figures 7(a) and 7(c) show, for the EOCCS $G/\kappa = 0.32$, the output spectrum of the optical high-order sidebands with the MCCSs $J/\kappa = 0$ and 0.006, respectively. As shown in Fig. 7(c), the amplitude of the OSS can be suppressed compared with that in Fig. 7(a). Furthermore, Figs. 7(b) and 7(d) show the output spectrum of the optical high-order sidebands with $J/\kappa = 0$ and 0.006, respectively, at the $G/\kappa = 0.8$. As also shown in Fig. 7(d), the amplitude of the OSS can be enhanced compared with that in Fig. 7(b). From the above analysis, these phenomena are consistent with the results in Fig. 6.

Before ending this section, we briefly discuss the possible experiment setup for the experimental techniques using a single small YIG crystal sphere, a 3D microwave cavity, and an optical cavity. The 3D microwave cavity is made of oxygen-free copper with inner dimensions of 44.0 × 20.0 × 6.0 mm^3. The optical cavity consists of two mirrors. The YIG sphere located at the central intersection of the microwave and optical cavities is highly polished from pure single-crystal YIG. The magnon frequency $\omega_m = 6.75$ GHz is determined by the bias magnetic field H and gyromagnetic ratio $\gamma/2\pi = 28$ GHz/T, with $\omega_m = \gamma H$. So the bias magnetic field $H \approx 38$ mT. The YIG sphere has the Verdet constant $\nu = 3.77$ rad/cm, the refractive index $n_r = 2.19$, and the spin density $n_{\text{spin}} = 2.1 \times 10^{28}\ \text{m}^{-3}$. Other feasible parameters are $P_d = P_c = 15$ mW, $P_m = 0.05$ μW, $\lambda_d = 1550$ nm, $2\kappa_m = 1$ MHz, $2\kappa_b = 15$ MHz, and $2\kappa_c/2\pi = 3.3$ MHz. The above parameters are mostly based on Refs. [9,19,20,22]. For cavity optomagnonics, the strength of the coupling between light and magnetic material is important for the frequency conversion of the sideband. The volume V_{sp} of YIG affects the EOCCS, i.e., $G = g_{abm}\alpha$ [19]. The average amplitude of the TM optical field $\alpha = \sqrt{\frac{2}{\kappa_a}\frac{P_a}{\hbar\omega_a}}$ [51]. For example, considering a 200-μm-diam YIG sphere, if $P_d = P_a$, $\kappa_a = \kappa_b$, and $\lambda_a = \lambda_d$, then G can reach approximately 43 MHz. Furthermore, $J = g_s\sqrt{n_{\text{spin}}V_{\text{sp}}}$ [45], with $g_s/2\pi = 39$ mHz [7]. For example, considering a 200-μm-diam YIG sphere, J can reach approximately 72 MHz. In this article, the values of G and J are taken in accordance with the above taken limits. We believe that the proposed structure is experimentally realizable and deserves to be explored using the present experimental technique.

IV. CONCLUSION

In summary, we have presented a scheme for optical sideband generation via the nonlinear magnon in a hybrid cavity-optomagnonical system consisting of a single small YIG crystal sphere, a microwave cavity, and an optical cavity. We obtained analytical expressions of the OSS generation by solving the nonlinear Heisenberg-Langevin equations using a perturbation method. It was demonstrated that the overlap between the first- and second-order spectra gradually increases with the increase of the EOCCS within the experimental parameter range, and the number of peaks in the OSS spectra changes from 2 to 4. Furthermore, the results have shown that the OSS exhibits a maximum value as the EOCCS increases and the MCCS can regulate the size and location of the maximum value of the OSS. Our research may have important implications in the modulation of microwave-optical conversion and higher-precision measurement.

ACKNOWLEDGMENT

The authors gratefully acknowledge the project funded by the National Natural Science Foundation of China (Grant No. 11874251).

APPENDIX: EXPLICIT EXPRESSION FOR $O_1^+(O_2^+)$

Substituting δo into Eqs. (10)–(12), we can get O_1^+ as

$$M_1^+ = \frac{-2iK(m_s)^2(M_1^-)^*}{f(i\Delta_p)}, \tag{A1}$$

$$B_1^+ = \frac{iGM_1^+}{\delta(-i\Delta_p)}, \tag{A2}$$

$$C_1^+ = \frac{iJM_1^+}{-i\Delta_c - \kappa_c - i\Delta_p}. \tag{A3}$$

We can also solve the equations and obtain O_2^+ as

$$M_2^+ = \frac{-2iK[2m_s(M_1^-)^* M_1^+ + (m_s)^*(M_1^+)^2]}{f(2i\Delta_p)} - \frac{2iK(m_s)^2(M_2^-)^*}{f(2i\Delta_p)}, \tag{A4}$$

$$B_2^+ = \frac{iGM_2^+}{\delta(-2i\Delta_p)}, \tag{A5}$$

$$C_2^+ = \frac{iJM_2^+}{-i\Delta_c - \kappa_c - 2i\Delta_p}. \tag{A6}$$

---

[1] K. Wang, Y.-P. Gao, R. Jiao, and C. Wang, Recent progress on optomagnetic coupling and optical manipulation based on cavity-optomagnonics, Front. Phys. **17**, 42201 (2022).

[2] H. Yuan, Y. Cao, A. Kamra, R. A. Duine, and P. Yan, Quantum magnonics: When magnon spintronics meets quantum information science, Phys. Rep. **965**, 1 (2022).

[3] D. Lachance-Quirion, Y. Tabuchi, A. Gloppe, K. Usami, and Y. Nakamura, Hybrid quantum systems based on magnonics, Appl. Phys. Express **12**, 070101 (2019).

[4] A. A. Serga, A. V. Chumak, and B. Hillebrands, YIG magnonics, J. Phys. D **43**, 264002 (2010).

[5] J. Rao, S. Kaur, B. Yao, E. Edwards, Y. Zhao, X. Fan, D. Xue, T. J. Silva, Y. Gui, and C.-M. Hu, Analogue of dynamic Hall effect in cavity magnon polariton system and coherently controlled logic device, Nat. Commun. **10**, 2934 (2019).

[6] T. Wolz, A. Stehli, A. Schneider, I. Boventer, R. Macêdo, A. V. Ustinov, M. Kläui, and M. Weides, Introducing coherent time control to cavity magnon-polariton modes, Commun. Phys. **3**, 3 (2020).

[7] Y. Tabuchi, S. Ishino, T. Ishikawa, R. Yamazaki, K. Usami, and Y. Nakamura, Hybridizing ferromagnetic magnons and microwave photons in the quantum limit, Phys. Rev. Lett. **113**, 083603 (2014).

[8] D. Zhang, X.-M. Wang, T.-F. Li, X.-Q. Luo, W. Wu, F. Nori, and J. You, Cavity quantum electrodynamics with ferromagnetic magnons in a small yttrium-iron-garnet sphere, npj Quantum Inf. **1**, 15014 (2015).

[9] Y.-P. Wang, G.-Q. Zhang, D. Zhang, X.-Q. Luo, W. Xiong, S.-P. Wang, T.-F. Li, C.-M. Hu, and J. Q. You, Magnon Kerr effect in a strongly coupled cavity-magnon system, Phys. Rev. B **94**, 224410 (2016).

[10] Y.-P. Wang, G.-Q. Zhang, D. Zhang, T.-F. Li, C.-M. Hu, and J. Q. You, Bistability of cavity magnon polaritons, Phys. Rev. Lett. **120**, 057202 (2018).

[11] D. Zhang, X.-Q. Luo, Y.-P. Wang, T.-F. Li, and J. You, Observation of the exceptional point in cavity magnon-polaritons, Nat. Commun. **8**, 1368 (2017).

[12] G.-Q. Zhang and J. Q. You, Higher-order exceptional point in a cavity magnonics system, Phys. Rev. B **99**, 054404 (2019).

[13] J. Zhao, Y. Liu, L. Wu, C.-K. Duan, Y.-X. Liu, and J. Du, Observation of anti-$\mathcal{PT}$-symmetry phase transition in the magnon-cavity-magnon coupled system, Phys. Rev. Appl. **13**, 014053 (2020).

[14] Y. Yang, Y.-P. Wang, J. W. Rao, Y. S. Gui, B. M. Yao, W. Lu, and C.-M. Hu, Unconventional singularity in anti-parity-time symmetric cavity magnonics, Phys. Rev. Lett. **125**, 147202 (2020).

[15] B. Wang, C. Kong, Z.-X. Liu, H. Xiong, and Y. Wu, Magnetic-field-controlled magnon chaos in an active cavity-magnon system, Laser Phys. Lett. **16**, 045208 (2019).

[16] M. Harder, Y. Yang, B. M. Yao, C. H. Yu, J. W. Rao, Y. S. Gui, R. L. Stamps, and C.-M. Hu, Level attraction due to dissipative magnon-photon coupling, Phys. Rev. Lett. **121**, 137203 (2018).

[17] Y.-P. Wang, J. W. Rao, Y. Yang, P.-C. Xu, Y. S. Gui, B. M. Yao, J. Q. You, and C.-M. Hu, Nonreciprocity and unidirectional invisibility in cavity magnonics, Phys. Rev. Lett. **123**, 127202 (2019).

[18] T. Liu, X. Zhang, H. X. Tang, and M. E. Flatté, Optomagnonics in magnetic solids, Phys. Rev. B **94**, 060405(R) (2016).

[19] A. Osada, R. Hisatomi, A. Noguchi, Y. Tabuchi, R. Yamazaki, K. Usami, M. Sadgrove, R. Yalla, M. Nomura, and Y. Nakamura, Cavity optomagnonics with spin-orbit coupled photons, Phys. Rev. Lett. **116**, 223601 (2016).

[20] X. Zhang, N. Zhu, C.-L. Zou, and H. X. Tang, Optomagnonic whispering gallery microresonators, Phys. Rev. Lett. **117**, 123605 (2016).

[21] J. A. Haigh, A. Nunnenkamp, A. J. Ramsay, and A. J. Ferguson, Triple-resonant Brillouin light scattering in magneto-optical cavities, Phys. Rev. Lett. **117**, 133602 (2016).

[22] R. Hisatomi, A. Osada, Y. Tabuchi, T. Ishikawa, A. Noguchi, R. Yamazaki, K. Usami, and Y. Nakamura, Bidirectional conversion between microwave and light via ferromagnetic magnons, Phys. Rev. B **93**, 174427 (2016).

[23] N. Zhu, X. Zhang, X. Han, C.-L. Zou, C. Zhong, C.-H. Wang, L. Jiang, and H. X. Tang, Waveguide cavity optomagnonics for microwave-to-optics conversion, Optica **7**, 1291 (2020).

[24] Y. S. Ihn, S.-Y. Lee, D. Kim, S. H. Yim, and Z. Kim, Coherent multimode conversion from microwave to optical wave via a magnon-cavity hybrid system, Phys. Rev. B **102**, 064418 (2020).

[25] Z. Shen, G.-T. Xu, M. Zhang, Y.-L. Zhang, Y. Wang, C.-Z. Chai, C.-L. Zou, G.-C. Guo, and C.-H. Dong, Coherent coupling between phonons, magnons, and photons, Phys. Rev. Lett. **129**, 243601 (2022).

[26] Z.-B. Yang, J.-S. Liu, H. Jin, Q.-H. Zhu, A.-D. Zhu, H.-Y. Liu, Y. Ming, and R.-C. Yang, Entanglement enhanced by Kerr nonlinearity in a cavity-optomagnonics system, Opt. Express **28**, 31862 (2020).

[27] Q. Cai, J. Liao, and Q. Zhou, Stationary entanglement between light and microwave via ferromagnetic magnons, Ann. Phys. (Berlin) **532**, 2000250 (2020).

[28] Q. Cai, J. Liao, B. Shen, G. Guo, and Q. Zhou, Microwave quantum illumination via cavity magnonics, Phys. Rev. A **103**, 052419 (2021).

[29] D. Kong, J. Xu, C. Gong, F. Wang, and X. Hu, Magnon-atom-optical photon entanglement via the microwave photon-mediated raman interaction, Opt. Express **30**, 34998 (2022).

[30] H. Xiong, L.-G. Si, A.-S. Zheng, X. Yang, and Y. Wu, Higher-order sidebands in optomechanically induced transparency, Phys. Rev. A **86**, 013815 (2012).

[31] T. Udem, R. Holzwarth, and T. W. Hänsch, Optical frequency metrology, Nature (London) **416**, 233 (2002).

[32] M.-A. Miri, G. D'Aguanno, and A. Alù, Optomechanical frequency combs, New J. Phys. **20**, 043013 (2018).

[33] Z.-X. Liu and Y.-Q. Li, Optomagnonic frequency combs, Photon. Res. **10**, 2786 (2022).

[34] Z. Wang, H. Y. Yuan, Y. Cao, Z.-X. Li, R. A. Duine, and P. Yan, Magnonic frequency comb through nonlinear magnon-skyrmion scattering, Phys. Rev. Lett. **127**, 037202 (2021).

[35] T. Hula, K. Schultheiss, F. J. T. Goncalves, L. Körber, M. Bejarano, M. Copus, L. Flacke, L. Liensberger, A. Buzdakov, A. Kákay *et al.*, Spin-wave frequency combs, Appl. Phys. Lett. **121**, 112404 (2022).

[36] H. Suzuki, E. Brown, and R. Sterling, Nonlinear dynamics of an optomechanical system with a coherent mechanical pump: Second-order sideband generation, Phys. Rev. A **92**, 033823 (2015).

[37] S. Liu, W.-X. Yang, Z. Zhu, T. Shui, and L. Li, Quadrature squeezing of a higher-order sideband spectrum in cavity optomechanics, Opt. Lett. **43**, 9 (2018).

[38] Z.-X. Liu, B. Wang, H. Xiong, and Y. Wu, Magnon-induced high-order sideband generation, Opt. Lett. **43**, 3698 (2018).

[39] W.-L. Xu, Y.-P. Gao, T.-J. Wang, and C. Wang, Magnon-induced optical high-order sideband generation in hybrid atom-cavity optomagnonical system, Opt. Express **28**, 22334 (2020).

[40] Y. Liu, L. Ling, T. Shui, N. Ji, S. Liu, and W.-X. Yang, Two-color second-order sideband generation via magnon Kerr nonlinearity in a cavity magnonical system, J. Opt. Soc. Am. B **39**, 1042 (2022).

[41] Z. Wu, W.-X. Yang, L. Li, X. Li, and X. Wang, Enhanced second-order sideband via surface plasmon polaritons in a low-Q microcavity, J. Appl. Phys. **131**, 053103 (2022).

[42] B. Zaks, R.-B. Liu, and M. S. Sherwin, Experimental observation of electron-hole recollisions, Nature (London) **483**, 580 (2012).

[43] X.-T. Xie, B.-F. Zhu, and R.-B. Liu, Effects of excitation frequency on high-order terahertz sideband generation in semiconductors, New J. Phys. **15**, 105015 (2013).

[44] M. Aspelmeyer, T. J. Kippenberg, and F. Marquardt, Cavity optomechanics, Rev. Mod. Phys. **86**, 1391 (2014).

[45] G. Zhang, Y. Wang, and J. You, Theory of the magnon Kerr effect in cavity magnonics, Sci. China Phys. Mech. Astron. **62**, 987511 (2019).

[46] S. Sharma, Y. M. Blanter, and G. E. W. Bauer, Light scattering by magnons in whispering gallery mode cavities, Phys. Rev. B **96**, 094412 (2017).

[47] A. Osada, A. Gloppe, Y. Nakamura, and K. Usami, Orbital angular momentum conservation in Brillouin light scattering within a ferromagnetic sphere, New J. Phys. **20**, 103018 (2018).

[48] S. Weis, R. Rivière, S. Deléglise, E. Gavartin, O. Arcizet, A. Schliesser, and T. J. Kippenberg, Optomechanically induced transparency, Science **330**, 1520 (2010).

[49] H. Xiong, L.-G. Si, and Y. Wu, Precision measurement of electrical charges in an optomechanical system beyond linearized dynamics, Appl. Phys. Lett. **110**, 171102 (2017).

[50] Y. A. Kosevich, L. I. Manevitch, and A. V. Savin, Wandering breathers and self-trapping in weakly coupled nonlinear chains: Classical counterpart of macroscopic tunneling quantum dynamics, Phys. Rev. E **77**, 046603 (2008).

[51] A. Rueda, W. Hease, S. Barzanjeh, and J. M. Fink, Electro-optic entanglement source for microwave to telecom quantum state transfer, npj Quantum Inf. **5**, 108 (2019).

Correction: An affiliation for the first author was missing and has been inserted as the second affiliation. The subsequent affiliation has been renumbered.